PAPER

Global and pedestal confinement and pedestal structure in dimensionless collisionality scans of low-triangularity H-mode plasmas in JET-ILW

To cite this article: L. Frassinetti *et al* 2017 *Nucl. Fusion* **57** 016012

IOP Publishing | International Atomic Energy Agency Nuclear Fusion

Nucl. Fusion **57** (2017) 016012 (16pp) doi:10.1088/0029-5515/57/1/016012

Global and pedestal confinement and pedestal structure in dimensionless collisionality scans of low-triangularity H-mode plasmas in JET-ILW

L. Frassinetti[1], M.N.A. Beurskens[2,3], S. Saarelma[3], J.E. Boom[4], E. Delabie[5], J. Flanagan[3], M. Kempenaars[3], C. Giroud[3], P. Lomas[3], L. Meneses[6], C.S. Maggi[3], S. Menmuir[3], I. Nunes[6], F. Rimini[3], E. Stefanikova[1], H. Urano[7], G. Verdoolaege[8,9] and JET Contributors[a]

EUROfusion Consortium, JET, Culham Science Centre, Abingdon, OX14 3DB, UK
[1] Division of Fusion Plasma Physics, KTH Royal Institute of Technology, Stockholm, SE, Sweden
[2] Max-Planck-Institut für Plasmaphysik, D-17491 Greifswald, Germany
[3] CCFE, Culham Science Centre, Abingdon, OX14 3DB, UK
[4] Max-Planck-Institut für Plasmaphysik, Boltzmannstr.2, 85748 Garching, Germany
[5] Oak Ridge National Laboratory, Oak Ridge, TN 37831-6169 USA
[6] Instituto de Plasmas e Fusão Nuclear, IST, Universidade de Lisboa, 1049-001 Lisboa, Portugal
[7] Japan Atomic Energy Agency, Naka Fusion Institute, Naka, 311-0193, Japan
[8] Department of Applied Physics, Ghent University Sint-Pietersnieuwstraat 41 B-9000 Ghent, Belgium
[9] Laboratory for Plasma Physics—Royal Military Academy (LPP-ERM/KMS), Avenue de la Renaissancelaan 30, B-1000 Brussels, Belgium

E-mail: lorenzo.frassinetti@ee.kth.se

Received 3 February 2016, revised 6 September 2016
Accepted for publication 8 September 2016
Published 11 October 2016

Abstract

A dimensionless collisionality scan in low-triangularity plasmas in the Joint European Torus with the ITER-like wall (JET-ILW) has been performed. The increase of the normalized energy confinement (defined as the ratio between thermal energy confinement and Bohm confinement time) with decreasing collisionality is observed. Moreover, at low collisionality, a confinement factor H_{98}, comparable to JET-C, is achieved. At high collisionality, the low normalized confinement is related to a degraded pedestal stability and a reduction in the density-profile peaking.

The increase of normalized energy confinement is due to both an increase in the pedestal and in the core regions. The improvement in the pedestal is related to the increase of the stability. The improvement in the core is driven by (i) the core temperature increase via the temperature-profile stiffness and by (ii) the density-peaking increase driven by the low collisionality.

Pedestal stability analysis performed with the ELITE (edge-localized instabilities in tokamak equilibria) code has a reasonable qualitative agreement with the experimental results. An improvement of the pedestal stability with decreasing collisionality is observed. The improvement is ascribed to the reduction of the pedestal width, the increase of the bootstrap current and the reduction of the relative shift between the positions of the pedestal density and pedestal temperature.

The EPED1 model predictions for the pedestal pressure height are qualitatively well correlated with the experimental results. Quantitatively, EPED1 overestimates the

[a] See the appendix of [94].

experimental pressure by 15–35%. In terms of the pedestal width, a correct agreement (within 10–15%) between the EPED1 and the experimental width is found at low collisionality. The experimental pedestal width increases with collisionality. Nonetheless, an extrapolation to low-collisionality values suggests that the width predictions from the KBM constraint are reasonable for ITER.

Keywords: JET-ILW, confinement, collisionality, pedestal, stability

(Some figures may appear in colour only in the online journal)

1. Introduction

The baseline type I ELMy H-mode scenario was re-established in JET with the new tungsten divertor and beryllium main wall (JET-ILW) in 2011 [1, 2]. The initial results showed a confinement degradation of the ITER baseline scenarios with a confinement factor in the range $H_{98} \approx 0.8$–0.9 [3, 4] compared to $H_{98} \approx 1.0$ in the carbon-wall JET (JET-C). H_{98} is the ratio between the energy confinement and the energy confinement expected by the IPB98(y,2) scaling [5]. This has been attributed, at least in part, to the achievable operational space obtained in the initial JET-ILW campaigns which was restricted to high plasma density to reduce W accumulation in the core [4, 6–8]. The degraded confinement was mainly driven by a lower pedestal pressure due to a pedestal temperature approximately 20–30% lower than in JET-C. Moreover, while JET-C has achieved a better confinement at high triangularity than at low triangularity due to an improved pedestal stability [9–11], JET-ILW in the baseline scenario has not yet shown any major difference between the low and the high shape [4, 12]. To date, a better confinement at high triangularity has been achieved only by N_2 seeding [3]. The N_2 injection has led to a pedestal behaviour comparable to JET-C, both in terms of pedestal pressure height [13] and in terms of ELM energy losses and timescale of the ELM crash [14].

The metal wall has also produced confinement degradation in ASDEX Upgrade (AUG) [15]. Recently, the energy confinement degradation in the metal wall AUG was attributed to the high deuterium puff rate [16]. The metal wall AUG tends to have higher collisionality than the carbon wall AUG, but a recent comparative study in low-triangularity plasmas [16] has shown that similar pedestal pressures can be achieved when deuterium is not puffed.

Recent results obtained in the JET-ILW baseline scenario show that $H_{98} \approx 1$ can be obtained at low triangularity when the outer strike point is moved from the horizontal target to the divertor corner, near the pump duct, where lower pedestal density, higher pedestal temperature (so lower collisionality, ν^*), can be reached [12, 17, 18]. The improvement was mainly driven by the increase in the core-stored energy and not in the pedestal stored energy. In the core, the reduced collisionality led to an increased density peaking and the temperature profile stiffness led to an increased core temperature. These two effects led to an increased core-stored energy [18]. However, it was not possible to extract conclusive information on the role of collisionality in confinement and in pedestal stability because both the normalized plasma pressure (β) and the normalized ion Larmor radius (ρ^*) were not constant. In particular, ρ^* strongly affects the normalized energy confinement (defined as the ratio between thermal energy confinement and Bohm confinement time) [19]. Indeed, the observations from the initial JET-ILW campaign might suggest that the collisionality has an important role in the confinement. In particular, JET-ILW plasmas tend to have higher collisionality than the baseline JET-C plasmas [4]. However, a dimensionless collisionality scan (with the other dimensionless parameters constant) has not been performed yet in JET-ILW and the role of collisionality in the normalized energy confinement and pedestal stability is not yet fully understood. ITER will operate at low collisionality. So, the scaling of the normalized energy confinement and of the pedestal stability with collisionality are important to predict ITER performances.

The present work investigates the role of the collisionality on the normalized energy confinement and on the pedestal stability in a dimensionless collisionality scan. Dimensionless scans are commonly used in tokamak physics to compare transport and confinement among different machines and to extrapolate the present day experiments to ITER [19]. The normalized energy confinement time can be expressed in terms of several dimensionless parameters (see for example [19–21]):

$$\frac{\tau_E}{\tau_B} \propto \rho^{*-\alpha_\rho}\, \beta^{-\alpha_\beta}\, \nu^{*-\alpha_\nu}\, M^{-\alpha_M}\, q^{-\alpha_q}\, \varepsilon^{-\alpha_\epsilon}\, \kappa^{-\alpha_\kappa}\, Z_{eff}^{-\alpha_Z}\, M_{rot}^{-\alpha_{M_{rot}}} \left(\frac{T_i}{T_e}\right)^{-\alpha_T} \quad (1)$$

where τ_E is the energy confinement time (defined as the thermal stored energy divided by the input power), $\tau_B = a^2 B/T \propto \rho^{*-2} B^{-1}$ is the Bohm confinement time (with a the minor radius, B the magnetic field and T the temperature), ρ^* is the normalized ion Larmor radius, β is the plasma thermal pressure normalized to the magnetic field pressure, ν^* is the ratio of the collision frequency over the trapped electron-bounce frequency, M the ratio of the ion mass over the proton mass, q the safety factor, ε the inverse aspect ratio, κ the elongation, Z_{eff} the effective charge, M_{rot} is the Mach number and T_i/T_e the ratio of the ion temperature over the electron temperature. Typically, in dimensionless scaling studies, equation (1) is simplified by expressing the Bohm confinement as a function of ρ^* and B in order to reach the expression:

$$B\tau_E \propto \rho^{*-2-\alpha_\rho}\, \nu^{*-\alpha_\nu}\, \beta^{*-\alpha_\beta} \quad (2)$$

(here, only the ρ^*, ν^* and β terms have been retained for simplicity).

Part of the scaling exponents in equation (1) can be estimated from the IPB98(y, 2) scaling [5] obtaining $\alpha_\rho = 2.7$, $\alpha_\beta = 0.9$, $\alpha_\nu = 0.01$, $\alpha_q = 3$. The IPB98(y, 2) scaling shows no dependence on ν^*, however, in [5] the IPB98(y) scaling shows a stronger dependence, with $\alpha_\nu \approx 0.1$. This suggests that the scaling of specific parameters is not easy to assess. So, devoted dimensionless scans have tried to determine in detail the scaling exponents. In some cases, a good agreement with the IPB98(y, 2) scaling was obtained, as for the ρ^* scan [22–26]. In other cases a disagreement was obtained, as for the ν^* and β scans [25, 27–31]. A detailed review on devoted dimensionless scans is presented in [19] and discussions on the disagreements are presented in [26, 28, 32].

In JET-C, the devoted dimensionless collisionality scan has shown an increase of the normalized confinement with decreasing collisionality, $B\tau_E \sim \nu^{*-0.35}$ [28]. The increase of the normalized energy confinement with decreasing collisionality has also been observed in other devices, such as Alcator C-Mod [24], DIII-D [27], JT60-U [25], MAST [31] and NSTX [33]. In JET-C, the correlation between collisionality and confinement has been briefly discussed, recently [11] and, for the baseline scenario, a weak negative trend between H_{98} and collisionality has been observed. The trend was mainly ascribed to the increased pressure peaking due to increased density peaking with decreasing collisionality. The dependence of density peaking with collisionality is predicted by IGT/TEM (ion temperature gradient/trapped-electron mode) theory (see, for example, [34]) and has been experimentally observed in many devices [35–39]. It should be pointed out that the dataset used for JET-C in [11] does not have the other dimensionless parameters constant, so no clear conclusions on the collisionality scaling could be drawn. More recently, a comparison of JET-C and JET-ILW global and pedestal confinement was discussed in [4], but without investigating the role of collisionality.

The pedestal plays a major role in fusion. For example, the fusion power produced in future tokamak reactors is expected to be strongly dependent on the pressure at the top of the pedestal [40]. Understanding the behaviour of the pedestal structure is important for ITER, where a pedestal temperature of approximately 4 keV is necessary to achieve its fusion power target [41]. The height of the pedestal pressure is determined by the interplay between the pedestal pressure gradient and the pedestal pressure width. The behaviour of the pressure gradient is, typically, reasonably described by the peeling-ballooning stability [42–48]. However, part of the recent results show that under some conditions the JET-ILW plasma in the pre-ELM phase might not have reached the peeling-ballooning stability limit yet and the modelled normalized pressure gradient tends to overestimate the experimental one [4, 18, 49]. Recent results in AUG-W also suggest a behaviour similar to JET-ILW [50].

The behaviour of the pressure width is often described as in the EPED1 model [51] which, based on the kinetic ballooning mode (KBM) constraint and empirical trends, expects $w_{pe} \sim (\beta_p^{ped})^{0.5}$, where w_{pe} is the pressure pedestal width in poloidal flux (normalized to one at the separatrix) and β_p^{ped} is the poloidal beta at the top of the pedestal. Several results from different experimental machines are consistent with this scaling [18, 51–56]. Inconsistencies with the KBM constraint have been observed in NSTX [46, 57], AUG [54] and JET-ILW [58]. Note that the effect of the other dimensionless parameters is not considered in the KBM constraint. Concerning the dependence with ρ^*, multi-machine studies performed in AUG, DIII-D and JET-C show a very weak or no dependence with the normalized Larmor radius [55, 59]. Concerning the dependence with ν^*, the DIII-D results [60] show a reduction of the density pedestal width at high density which is ascribed to the reduction of the neutral penetration length [61]. The JET-C results [62] show instead a positive trend between density pedestal width and density pedestal height. A similar behaviour has been recently observed in low current/low field JET-ILW plasmas [18]. Recent results from JT60-U also suggest a positive correlation of the pedestal width with the collisionality [63, 64].

To study the role of collisionality in the JET-ILW confinement, a set of dimensionless collisionality scans has been conducted in JET-ILW in baseline ELMy H-mode plasmas. In the present work, the volume-averaged collisionality is changed by a factor 5 and pedestal collisionality by a factor ≈10, while the other parameters in equation (1) are kept as constant as possible. This is further discussed in section 2.

This work describes the dependence of the normalized confinement of pedestal stability and pedestal structure on collisionality in JET-ILW. The experimental results are then compared with the peeling-ballooning stability and with the EPED1 model predictions. The paper is organized as follows. Section 2 describes the dataset used, discussing the dimensionless parameters and the corresponding operational parameters used. Section 3 describes the dependence of the normalized confinement on collisionality and the role of the core and pedestal. Section 4 describes the pedestal structure. Section 5 compares the experimental results with the EPED1 model. Section 6 discusses the peeling-ballooning stability. Section 7 describes the effect of collisionality on the scrape-off layer (SOL) density. Discussion and conclusions are presented in section 8.

2. Description of the database

2.1. Plasma scenario

The work has been carried out on a set of JET-ILW plasmas with β_N in the range ≈1.5–1.8. To date, differences in the confinement between high and low triangularity in the JET-ILW baseline scenario have been observed only with N_2 seeding [3, 13]. The present plasmas have been performed without N_2, so the low triangularity shape has been chosen for simplicity. The divertor configuration has the outer strike point on the divertor corner near the pump duct. This configuration allows operations at low Greenwald density (f_{GW} down to 0.55–0.6) and allows density control via gas puffing. The plasmas are heated mainly via NBI with a real-time control to achieve the desired β value. The neutral beam injection (NBI) power is in the range 11–22 MW. The ion cyclotron resonance heating

(ICRH) power is in the range 1–4 MW and is used to reduce W accumulation in the core.

The present plasmas are in a Type I ELMy H-mode as suggested by the increase of the edge-localized mode (ELM) frequency with the power through the separatrix. Moreover, the pedestal temperature T_e^{ped} is higher than 400–500 eV, while in JET-ILW the Type III ELMs occur at T_e^{ped} lower than 300 eV [4, 13]. Finally, the ELM energy losses are large compared to the Type III ELMs, with a value ($W_{ELM}/W_{ped} > 8$–10%) relatively consistent with Type-I ELM losses [14, 65]. The details of the ELM behaviour with collisionality will be discussed elsewhere.

2.2. Plasma parameters

The collisionality scan is achieved by changing the gas fuelling level. The normalized pressure and the normalized Larmor radius are kept constant by varying the NBI power and the plasma current. The magnetic field is changed in order to keep $q_{95} \approx 3$. Four collisionality scans have been achieved at four different β_N values. The volume-averaged collisionality ν^*, the volume-averaged normalized ion Larmor radius ρ^* and the normalized thermal beta β_N are shown in figures 1(*a*) and (*b*). The normalized collisionality ν^* (defined as the ion–electron collision rate normalized to the thermal ion-bounce frequency), the normalized ion Larmor radius ρ^* and the normalized thermal pressure have been calculated by volume-averaging the profiles using the following definitions:

$$\nu^* = 6.92 \cdot 10^{-18} n_e R q_{95} Z_{eff} \ln\Lambda / (\varepsilon^{3/2} T_e^2) \quad (3)$$

$$\rho^* = 4.57 \cdot 10^{-3} (2T_i)^{1/2} / (aB) \quad (4)$$

$$\beta = (p_e + p_i) / (B^2/2\mu_0) \quad (5)$$

where B is the magnetic field on the axis, a is the minor radius and p_e and p_i the electron and ion thermal pressure profiles, respectively. The thermal pressure is calculated assuming $T_i = T_e$ (as later discussed) and $n_i = n_e(5 - Z_{eff})/4$ (assuming beryllium as the main impurity). Note that since q_{95} is constant in the present datasets, β constant implies β_N constant (the normalized β, $\beta_N = \beta a B_T / I_p$).

The dataset is shown in figures 1(*a*) and (*b*). This is the dataset used to investigate the dependence of the normalized confinement on collisionality (section 3). The volume-averaged collisionality has been varied by a factor 5 from $\nu^* \approx 0.03$–0.04 to $\nu^* \approx 0.15$ for all the four β_N levels. The normalized Larmor radius is kept constant as much as possible in the range $\rho^* \approx 0.40\%$–0.45%. The variation in ρ^* is 12.5%, but it is not systematic versus ν^* and is mainly due to the fact that the low beta dataset has ρ^* lower than the high beta dataset ($\rho^* \approx 0.40\%$–0.42% at low β_N and $\rho^* \approx 0.43\%$–0.45% at high β_N). The effect of this variation in ρ^* will be discussed further in section 3 when discussing the scaling of the normalized energy confinement versus collisionality. The range of variation of all the dimensionless parameters is described in table 1.

The Mach number has been calculated as $M_{rot} = v_\phi / v_{th}$, where v_ϕ is the toroidal velocity and $v_{th} = \sqrt{eT_i/m}$ is the thermal velocity. It was not possible to keep the Mach number perfectly constant. The Mach number tends to be larger at low collisionality ($M_{rot} \approx 0.45$ *at* $\rho_{tor} = 0.5$) than at high collisionality ($M_{rot} \approx 0.3$ *at* $\rho_{tor} = 0.5$). A scaling analysis in JET-C [66] shows that the energy confinement scales as $\tau_E \propto (M_{rot})^{-0.21}$. Assuming a similar scaling in JET-ILW, the present difference in the Mach number would affect the energy confinement by ≈9% (much less than what was observed experimentally, from $\tau_E \approx 0.1$ s at high collisionality to $\tau_E \approx 0.25$ s–0.3 s at low collisionality). So, for the present dataset, it is reasonable to assume that the effect of M_{rot} is negligible compared to the effect of the collisionality.

The effective charge is measured with a line-integrated filter spectrometer. It was not possible to keep Z_{eff} constant throughout the entire scan, but the variation is relatively small, from $Z_{eff} \approx 1.2$ at high ν^* to $Z_{eff} \approx 1.5$ at low ν^*.

The ion temperature is similar to the electron temperature both in the core and at the pedestal with $T_i/T_e \approx 1.0$–1.05 and with no systematic variation versus ν^* (within the experimental uncertainty). This has been verified for two shots at low collisionality and two shots at high collisionality. The charge-exchange measurements are not available for the entire datasets.

The change in collisionality affects the density peaking and, therefore, also the ratio between core and pedestal pressure. This implies that, in a collisionality scan, a dataset with constant β_N has slightly different pedestal beta. This is shown in figure 1(*e*). For this reason, figures 1(*c*) and (*d*) show a second dataset which will be considered when investigating the pedestal structure (section 4). This dataset has been determined by considering the dimensionless parameters evaluated at the pedestal, ν^*_{ped}, ${\rho^*}_p^{ped}$ and β_p^{ped}, using expressions (3)–(5) with the temperature and the density evaluated at the pedestal. For the magnetic field, the poloidal field B_p has been used, where $B_p = \mu_0 I_p / c$ is poloidal magnetic field with c the length of the last closed flux surfaces. The pedestal collisionality ν^*_{ped} varies by a factor 10, while the pedestal-normalized Larmor radius is constant at ${\rho^*}_p^{ped} \approx 1.6$–$1.8\%$.

Using the definitions of the dimensionless parameters in equations (3)–(5) it is possible to express the temperature and the density as a function of ν^*, ρ^* and β:

$$n_e \sim \beta / {\rho^*}^2 \quad (6)$$

$$T_e \sim (q\beta/\nu^*)^{1/2} / \rho^* \quad (7)$$

(where $n_e = n_i$ is assumed for simplicity). It is clear that in a dimensionless collisionality scan the density does not change with ν^* [67]. So, a dimensionless collisionality scan might be interpreted as a pressure scan with constant density and constant q. Note that if the scan is performed using constant volume-averaged β and ρ^*, it is the volume-averaged density to remain constant. Due to the change in the density peaking with ν^*, this implies the increase of the core density and the reduction of the pedestal density with decreasing ν^*. On the

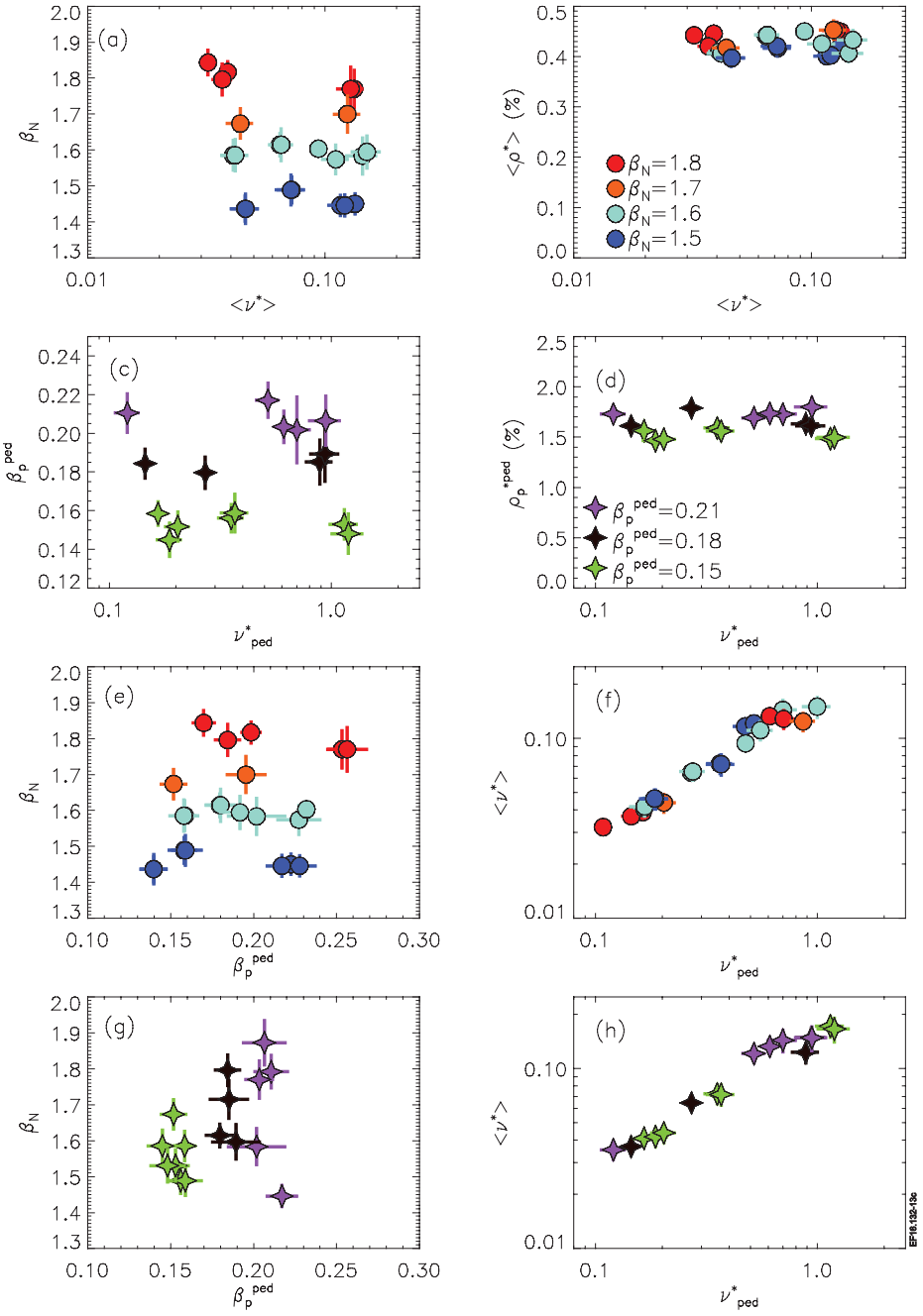

Figure 1. Range of the dimensionless parameters. Frames (*a*) and (*b*) show the range of variation of the volume-averaged collisionality, normalized beta and volume-averaged Larmor radius. The colours highlight four different collisionality scans achieved at different β_N values. This dataset is used to study the global confinement. Frames (*c*) and (*d*) show the range of variation of the pedestal collisionality, poloidal pedestal beta and pedestal Larmor radius. The colours highlight three different collisionality scans achieved at different β_p^{ped} values. This dataset is used to study the pedestal structure. Frames (*e*) and (*f*) show the normalized beta versus the pedestal beta for the dataset used in the study of the global confinement. Frames (*g*) and (*h*) show the normalized beta versus the pedestal beta for the dataset used in the study of the pedestal structure.

Table 1. Range of variation of the dimensionless parameters for the dataset used in the study of the global confinement (volume-averaged parameters are shown) and for the dataset used in the study of the pedestal structure (pedestal parameters are shown).

	ν^*	β	$\rho^*(10^{-3})$	M_{rot}	Z_{eff}	T_i/T_e
Average	0.03–0.15	1.45–1.84	0.40–0.45	0.3–0.45	1.25–1.55	1.0–1.05
Pedestal	0.1–1.0	0.14–0.22	1.5–1.8	0.2–0.3	1.25–1.55	1.0–1.05

Table 2. Range of variation of the operational parameters at low and high collisionality.

	I_p (MA)	q_{95}	P_{sep} (MW)	f_{GW}	Γ_{D2} 10^{22} (e s^{-1})
Low ν^*	2.5	2.9–3.1	9–16	0.6	1.0
High ν^*	1.7	2.9–3.1	15–22	0.8	5.0

Note: The ranges are relatively similar for both the global and the pedestal datasets.

other hand, if the scan is performed in the pedestal collisionality with constant pedestal β and constant pedestal ρ^*, it is the pedestal density to remain constant, while the core density increases with decreasing ν^*.

The main operational parameters are summarized in table 2. The plasma current is increased from $I_p \approx 1.7$ MA at high ν^* to $I_p \approx 2.5$ MA at low ν^*. The safety factor is approximately constant in the range $q_{95} = 2.9$–3.1. The power through the separatrix P_{sep} is in the range 9–22 MW. P_{sep} has been calculated as $P_{sep} = P_{NBI} + P_{\Omega} + P_{ICRH} - P_{rad,bulk} - dW/dt$. The Greenwald fraction is controlled via gas puff and increases from 0.6 at low ν^* to 0.8 at high ν^*. The gas flow injected from the valve used for density control is in the range $\Gamma_{D2} \approx 10^{22}$ (e/s) to $\Gamma_{D2} \approx 5 \cdot 10^{22}$ (e/s).

As a final remark, due to the fact that JET-C tends to have lower ν^*, higher β and significantly higher Z_{eff} than JET-ILW, it has not been possible to identify a set of JET-C plasma with dimensionless parameters similar to the present JET-ILW dataset. So a comparison between JET-C and JET-ILW cannot be discussed in the present paper.

2.3. Diagnostics for the pedestal structure

High-resolution Thomson scattering (HRTS) [68] is used to measure electron temperature and density. Only the profiles in a stationary phase are considered for the analysis of the pedestal structure. The stationary phases used are longer than 0.5s and at least four energy confinement times long ($\tau_E \approx$ 0.1 s–0.25 s). The pre-ELM density and temperature profiles of each stationary phase are then fitted with a modified hyperbolic tangent function [69] to estimate the pedestal height and pedestal width:

$$mtanh(r) = \frac{h}{2}\left(\frac{(1+sx)e^{x} - e^{-x}}{e^{x} + e^{-x}} + 1\right) \qquad \text{with} \quad x = \frac{p_{pos} - r}{2w_r} \tag{8}$$

where r is the radius in real space along the HRTS line of sight, h is the pedestal height, p_{pos} is the pedestal position and w_r the pedestal width in real space. The parameter s allows the presence of a linear slope in the inner side of the pedestal. The fits are performed in real space and then mapped on the poloidal flux normalized to one at the separatrix. The uncertainties in the pedestal parameters represent the errors on the parameters of the fits. These are in the range 2–8% for the pedestal height and 10–20% for the pedestal width.

Due to the uncertainty in the absolute position, the HRTS profiles are shifted accordingly to a two-point model for the power balance at the separatrix [70] in order to have a separatrix temperature, $T_e^{sep} \approx 100$ eV. The shift applied to the density is the same as that applied to the temperature. The shift is implemented systematically for all the profiles considered in this work.

In the SOL outside the separatrix, it is assumed that both density and temperature are negligible. This assumption works very well for the temperature and it is reasonable at medium and low collisionality for the density. At very high collisionality, the SOL density starts to no longer be negligible. This is further investigated in section 7, where the effect of a fitting function that allows $n_e^{SOL} \neq 0$ is discussed, showing that the impact on the pedestal width and gradient is minimal for the present dataset.

To estimate the pedestal width for the density and the temperature, only the profiles in the pre-ELM phase are considered. The fits are repeated considering the profiles in several pre-ELM phases in order to verify the stability of the result. In the fitting procedure, the effect of the HRTS instrument function is taken into account. The details of the HRTS fitting method are described in [71].

The electron pressure pedestal height is determined from the temperature and density pedestal height, $p_e^{ped} = k_B \cdot T_e^{ped} \cdot n_e^{ped}$. The pressure pedestal width is estimated using the definition implemented in EPED1, as the average between density and temperature pedestal widths, $w_{p_e} = (w_{n_e} + w_{T_e})/2$. The units of the pedestal width and of the pedestal position discussed in sections 4–6 are poloidal flux normalized to one at the separatrix.

The reflectometer data [72] are used to cross-check the density width estimations obtained with the HRTS. The reflectometer is available only for a limited set of data at low and medium collisionality, but generally the two diagnostics produce similar results within the experimental uncertainty. The Li-beam diagnostic is used to cross-check the HRTS data in the SOL. Further discussions are presented in section 7.

3. Normalized confinement and role of core and pedestal

3.1. Confinement factor and normalized confinement scaling

The initial results from the first JET-ILW campaigns have shown a reduction of the confinement in the baseline scenario with a confinement factor in the range $H_{98} = 0.8$–0.9 [4]. Good confinement with $H_{98} \approx 1.0$ has been recently recovered by moving the outer strike point on the divertor corner allowing operation at a lower density [12, 17, 18].

Figure 2(*a*) shows H_{98} versus β_N. The thin dashed line shows a linear fit to the low-collisionality shots ($\langle\nu^*\rangle < 0.05$) and the thick dashed line to the high collisionality ones ($\langle\nu^*\rangle > 0.1$). The JET-ILW plasmas at high ν^* show no dependence of H_{98} with β_N and the confinement factor remains at $H_{98} \approx 0.8$. A positive trend between H_{98} and β_N, as also observed in JET-C [11], is present at low ν^*. $H_{98} \approx 1.0$ is reached at low collisionality and high β_N.

The trend between H_{98} and ν^* is shown in figure 2(*b*). A clear increase of the confinement factor with decreasing ν^*

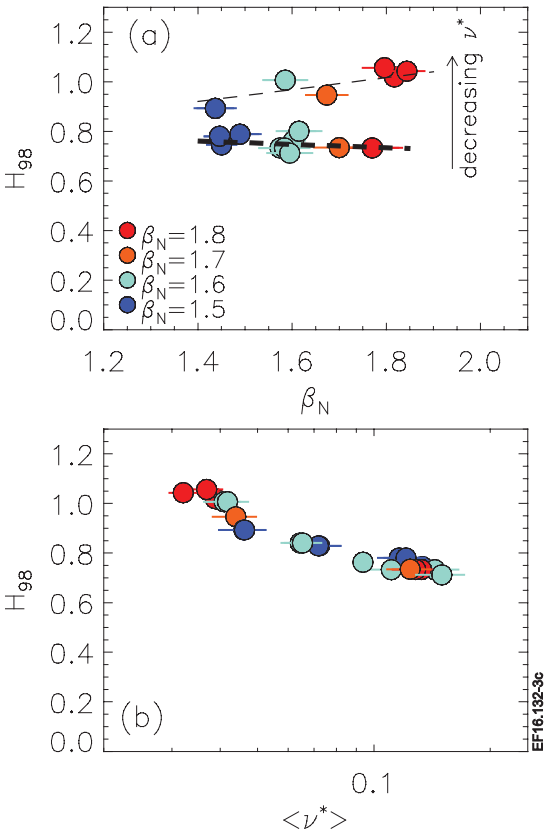

Figure 2. Correlation of H_{98} with β_N (*a*) and with volume-averaged ν^* (*b*). The dashed lines in frame (*a*) shows a linear fit to the data with low collisionality, $\nu^* < 0.05$ (thin dashed) and high collisionality, $\nu^* > 0.1$ (thick dashed).

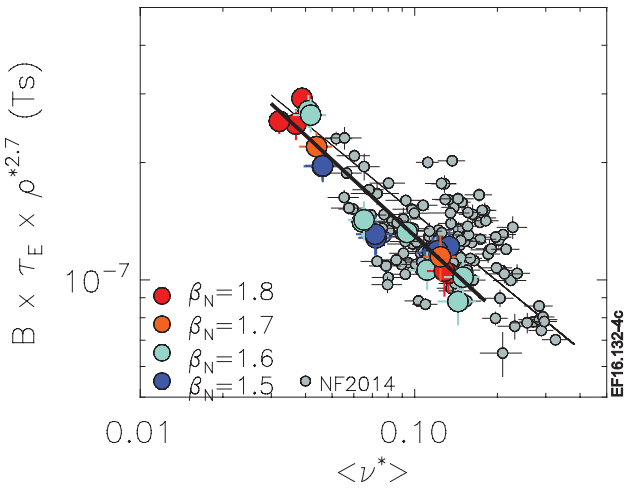

Figure 3. Correlation between the normalized confinement time and the collisionality. The thick line shows the fit to the present dataset. The thin line show the fit to the low-δ baseline JET-ILW dataset described in [4].

can be observed. Since the IPB98(y, 2) scaling suggests no dependence of the normalized confinement with collisionality, the trend of figure 2(*b*) suggests that the normalized confinement time increases with decreasing ν^*.

To study the scaling of the normalized energy confinement with collisionality, equation (2) is used. Figure 3 shows the results for the present dataset along with the low-δ baseline JET-ILW plasmas discussed in [4]. Note the dataset of [4] has no constant normalized Larmor radius ($\langle\rho^*\rangle$ varies in the range 0.27–0.42), no constant normalized pressure (β_N varies in the range 1.0–1.8) and no constant q_{95} (q_{95} = 2.5–4.5). The normalized energy confinement has a strong dependence with ρ^*, with a scaling $B\tau_E \sim \rho^{*-2.7}$ as determined in JET-C [26], in most of the tokamaks [19], and in the IPB98 scaling [5]. Therefore, the ρ^* dependence has been removed in figure 3. On the other hand, the β dependence of the normalized confinement is negligible, $\alpha_\beta \approx 0$ [29, 30] and should not affect the scaling. No estimations of the scaling exponent for the q_{95} dependence is available in JET, so it is not possible to remove any possible effect of q_{95} from the [4] dataset. In any case, no obvious systematic trend of β and q with ν^* were present in the [4] dataset. Another important difference between the two datasets is that the present one has the outer strike point near the divertor corner, while the [4] dataset has the outer strike point on the horizontal target.

In figure 3, the energy confinement time is calculated as the ratio between the total thermal stored energy and the input power. The thermal stored energy is determined by volume-integrating the pressure profile as described in [11]. By fitting the data of figure 3 using the expression of equation (8), the parameter α_ν is estimated as $\alpha_\nu = 0.6 \pm 0.1$ for the present dimensionless scan. Note that the present dataset has a clear overlap with the [4] dataset for $\nu^* > 0.05$. The scaling exponent for the dataset of [4] is $\alpha_\nu = 0.5 \pm 0.05$, which is consistent with the present estimation, within the error bars. This suggests that the strike point position does not have a major effect on the normalized confinement scaling with collisionality. However, due to the q_{95} variation in [4], no strong conclusions are possible. The present α_ν estimations is similar to those obtained in DIII-D [19, 27], but higher than those obtained in JET-C for which the exponent $\alpha_\nu \approx 0.35$ was determined [28, 73]. A more detailed discussion is presented in the last section.

3.2. Core and pedestal pressure and profile peaking

The increase of the normalized confinement with decreasing ν^* is related to an increase in both the core and in the pedestal region. Figure 4(*a*) shows the pedestal temperature T_e^{ped} versus the pedestal density n_e^{ped} and figure 4(*b*) the core temperature T_e^{core} versus the core density n_e^{core}. The reduction of ν^* is correlated to the reduction of n_e^{ped} and to the increase of T_e^{ped}. The increase of T_e^{ped} is stronger than the reduction of n_e^{ped} and, consequently, the low ν^* plasmas have higher electron pedestal pressure p_e^{ped}. The pedestal pressure increases by 70%, from $p_e^{ped} \approx 3.5$ kPa to $p_e^{ped} \approx 6$ kPa. In the core, a different behaviour is observed. The core density has a weak increase with decreasing ν^*, while the core temperature shows a strong increase. The increase in the core pressure is 150%, from $p_e^{ped} \approx 20$ kPa at high ν^* to $p_e^{ped} \approx 50$ kPa at low ν^*.

The stronger increase in the core pressure than in the pedestal pressure is correlated to the behaviour of the profile peaking, shown in figure 5.

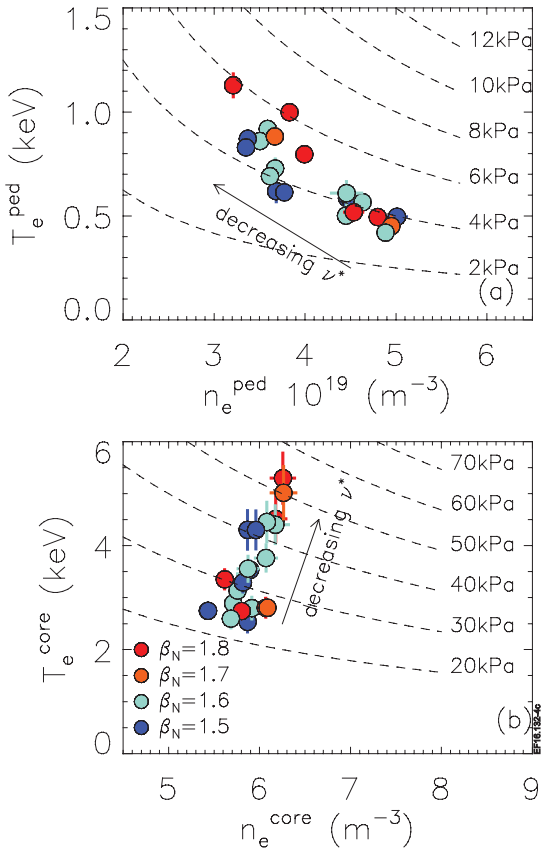

Figure 4. Pedestal temperature versus pedestal density (*a*) and core temperature versus core density (*b*). The core values are calculated at $\rho_{tor} = 0.3$, where ρ_{tor} is the square root of the normalized toroidal flux. The dashed lines show the isobar curves.

The density peaking versus $\langle\nu^*\rangle$ is shown in figure 5(*a*) and the temperature peaking versus $\langle\nu^*\rangle$ in figure 5(*b*). The density peaking scales very clearly with the collisionality, as already observed in several devices [4, 35–39, 74]. The temperature profiles are instead stiff and no clear dependence with collisionality is observed. This is consistent with earlier analysis in JET-ILW [4].

In summary, the increase of the core pressure is due to two factors: (i) the increase in T_e^{core} which is driven by the increase in T_e^{ped} via the T_e profile stiffness and (ii) the increase of the pressure peaking (figure 5(*c*)) due to the increase of the density peaking. The increase in the pedestal pressure is instead related to the improvement of the pedestal stability. The pedestal stability is discussed in sections 6.

4. Dependence of the pedestal structure on collisionality

The pedestal structure for a high and a low-collisionality shot at high beta is shown in figure 6. Note that, hereafter, the dataset with the dimensionless parameters matched at the pedestal top is used (second row in figure 1). Figure 6(*a*) shows the pedestal density, figure 6(*b*) the pedestal temperature and figure 6(*c*) the pedestal pressure. The reduction of collisionality does not affect the pedestal density height, see

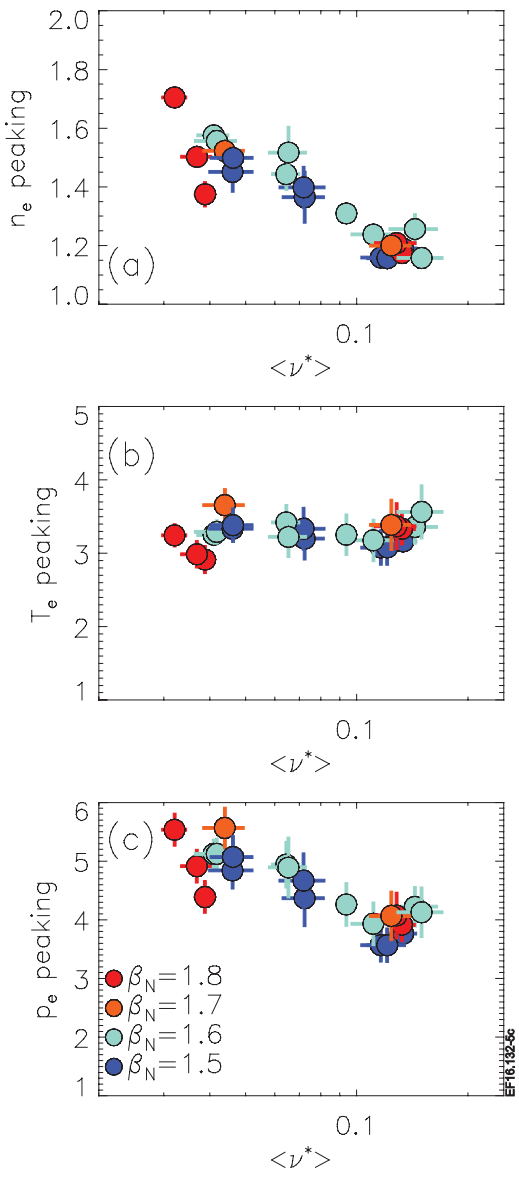

Figure 5. Density peaking (*a*) temperature peaking (*b*) and pressure peaking (*c*) versus the effective collisionality. The peaking is calculated as the profile at $\rho_{tor} = 0.3$ divided by the profiles at $\rho_{tor} = 0.8$.

equation (6), while the increase in the pedestal temperature height is observed. The overall effect is an increased pedestal pressure.

An important effect that can be observed in figure 6 is the reduction of the pedestal width with decreasing collisionality, both in the density, in the temperature and, consequently, in the pressure. A similar behaviour has been observed in JET-C during a gas scan in baseline plasmas [62] and in JT60-U in a collisionality scan [63, 64].

The behaviour of the pedestal pressure width for the entire dataset is shown in figure 7. To be consistent with the earlier width analysis and with the definition of width implemented in EPED, the pedestal pressure width has been calculated as the average between the density and the temperature width. For comparison, figure 7(*a*) shows the correlation between the

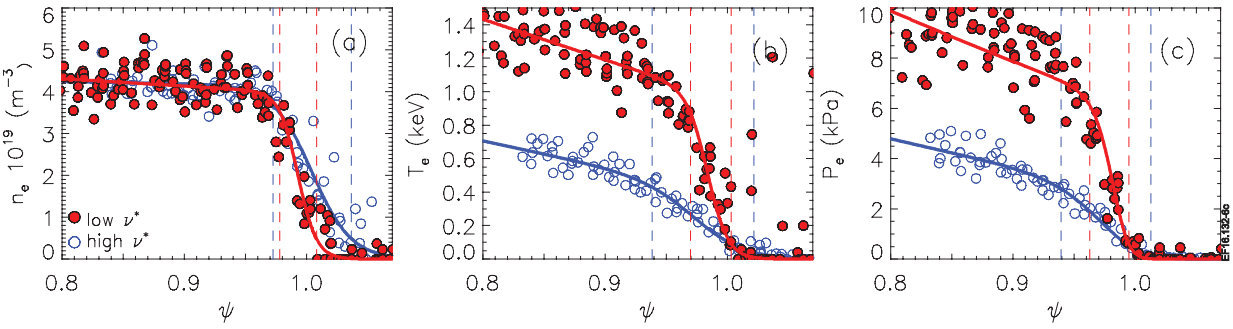

Figure 6. Pre-ELM profiles of electron density (*a*), temperature (*b*) and pressure (*c*) in the pedestal region for two plasmas with $\beta_p^{ped} \approx 0.21$ and $\rho_p^{*ped} \approx 1.7\%$ at low collisionality ($\nu_{ped}^* \approx 0.1$, red full dots) and high collisionality ($\nu_{ped}^* \approx 0.9$, blue empty dots). The vertical dashed lines highlight the pedestal width. The *x*-axis is the poloidal flux normalized to one at the separatrix.

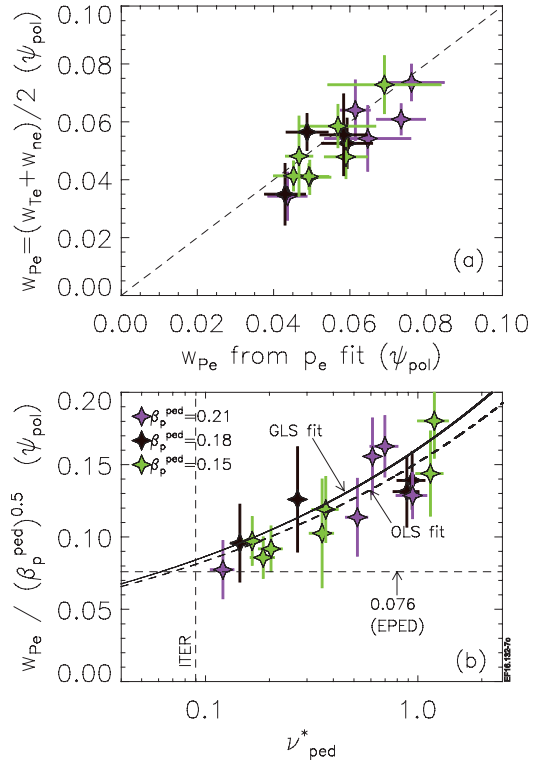

Figure 7. (*a*) Pressure pedestal width calculated as the average between the deconvolved density and temperature widths versus pressure width calculated from the non-deconvolved fit to the experimental pressure. The width is in normalized poloidal flux. (*b*) Pedestal pressure width with the β_p^{ped} dependence removed versus the pedestal collisionality.

pedestal pressure width calculated as average between temperature and density width versus the pedestal pressure width calculated by fitting the experimental pressure profiles. However, the latter (*x*-axis in figure 7(*a*)) is likely overestimating the real pressure width. In fact, techniques for the deconvolution of the Thomson scattering profiles to compensate the instrument function effect have been developed only for density and temperature, but not for pressure [71, 75]. So, on the *x*-axis of figure 7(*a*) the non-deconvolved pedestal width is used.

Table 3. Parameters of the non-linear regression of the pedestal pressure width with collisionality and beta.

	γ_ν	γ_β	c
OLS	0.26 ± 0.04	0.59 ± 0.27	0.19 ± 0.11
GLS	0.27 ± 0.05	0.71 ± 0.34	0.25 ± 0.16

Nonetheless, the two quantities are relatively well correlated within the error bars.

The correlation between pressure pedestal width and collisionality is shown in figure 7(*b*). Here, the width has been normalized to $(\beta_p^{ped})^{0.5}$ to remove the β dependence (the same trend implemented in EPED1 model). A positive trend between the pedestal width and the collisionality is present. However, at low collisionality, the present results reach values of pedestal width consistent within 10–15% with those expected in the EPED1 model, which according to an experimental scaling (qualitatively supported by the KBM model) assumes $w_{pe} = 0.076\sqrt{\beta_p^{ped}}$ [51]. This trend is often referred to as the KBM constraint. The discrepancy that is observed at high collisionality suggests that the present models are not sufficient to describe the pedestal width behaviour in detail.

The behaviour of the pressure width is relevant for pedestal height predictions, so a non-linear regression has been attempted using the following power law:

$$w_{pe} = c(\nu_{ped}^*)^{\gamma_\nu}(\beta_p^{ped})^{\gamma_\beta} \quad (9)$$

The regression has been done using ordinary least squares (OLS) and geodesic least squares (GLS) [76] using a bootstrapping method which employs a resampling technique that generates a large number of synthetic datasets from the original data, by resampling with replacement. Then, both OLS and GLS were carried out on each of these datasets and the average of all the obtained coefficients was calculated. The results are reported in table 3. As far as the dependence on collisionality is concerned, the two methods produce comparable results, with an exponent $\gamma_\nu \approx 0.26$. Concerning the scaling with β_p^{ped}, the OLS fit is relatively consistent with the scaling implemented in EPED (which assumes $\gamma_\beta = 0.5$), while the

GLS fit is somehow less consistent, estimating a stronger scaling with β_p^{ped}. However, the range of variation in β_p^{ped} is narrow and, given the large error bars, no strong conclusions on the width scaling with β_p^{ped} are possible.

Interestingly, the trend of the width versus collisionality might not have a major impact on ITER. The vertical dashed line shows the pedestal collisionality expected in ITER. This has been calculated with equation (3) using the values in [65] and assuming $Z_{eff} = 1.3$. No dependence of the pedestal width with ρ^* has been observed so far [55, 59], so the extrapolation to ITER might be reasonable even if the normalized Larmor radius is not considered. At ITER collisionality, no significant difference between the KBM constraint and the extrapolation of the experimental data is observed.

5. Comparison of the pedestal pressure with EPED1

To start investigating the effect of the collisionality on pedestal stability, a comparison of the experimental data with the EPED1 predictions has been performed for three shots at high beta ($\beta_p^{ped} \approx 0.21$) and with low, medium and high collisionality.

The comparison between the experimental pressure and the EPED1-predicted pressure is shown in figure 8. The inputs to EPED1 are the experimental pedestal density, the total beta, the plasma shape (R, a, κ, δ), the plasma current and the toroidal magnetic field [51]. The pedestal pressure height is calculated from the intersection of peeling-ballooning constraint (calculated with the ELITE code [42] using $\gamma > \omega^*_{max}/4$ as the stability criterion, where ω^*_{max} is the maximum of the ion diamagnetic frequency in the pedestal region) and the KBM constraint [51]. The intersection is found by creating self-consistent equilibria along the KBM constraint line that all have the same global beta (given as input) and then using the stability code to determine where the PB boundary is crossed. The pressure peaking varies from equilibrium to equilibrium. This is done to ensure that all equilibria have the same global beta. In this work, the bootstrap currents are calculated with the Koh model [77]. Figure 8(a) shows the pedestal pressure estimated with EPED1 versus the experimental p_e^{ped}. A good correlation is observed, but EPED1 tends to overestimate the experimental pedestal pressure. The overestimation increases with collisionality: at low ν^*_{ped} the difference is ≈15%, at medium and high ν^*_{ped} the EPED1 predictions are, respectively, ≈30% and ≈35% higher than the experimental results. The reason for the overestimation is a consequence of the fact that, often in JET-ILW, the operational points tend to be far from the PB boundary, as determined by ELITE and described in section 6.

The results in figure 8(a) might suggest that EPED1 predicts an improvement of the pedestal stability with decreasing collisionality, but this is not the case. This has been investigated by determining the normalized pressure gradient at the stability limit, α_{max} [78]:

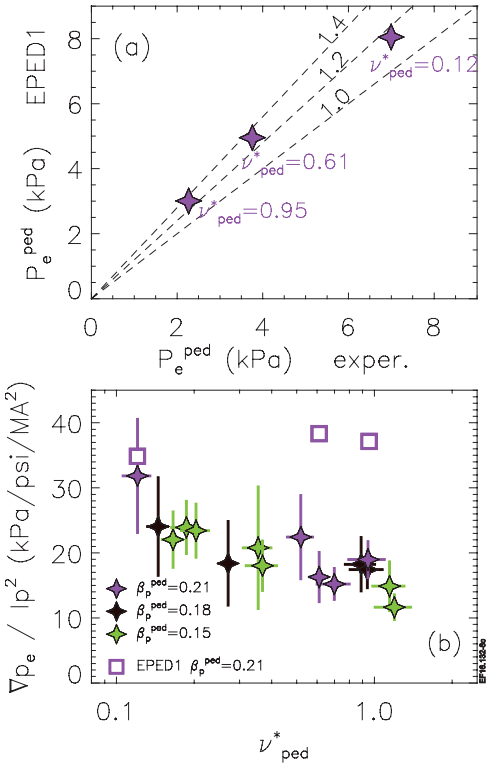

Figure 8. (a) Electron pedestal pressure height as estimated by EPED1 versus the experimental results. (b) pressure gradient normalized to plasma current square versus pedestal collisionality.

$$\alpha = -\frac{2\partial_\psi V}{(2\pi)^2}\left(\frac{V}{2\pi^2 R_0}\right)^{1/2}\mu_0 p' \qquad (10)$$

with V the plasma volume, R the major radius and p' the pressure derivative in the poloidal flux ψ. In this collisionality scan, EPED1 does not observe any significant change of α_{max}, which is in the range ≈4.2–4.4 both at low and high ν^*. So, EPED1 does not predict any improvement in the pedestal stability with decreasing collisionality.

The main parameters that affect the pedestal stability are the normalized pressure, the plasma shape, the pedestal width and the pedestal position of density and temperature. The three plasmas analysed with EPED1 have the same shape and similar normalized pressure. Moreover, EPED1 assumes no change in the pedestal widths (because β_p^{ped} is constant) and no difference in the pedestal position of density and temperature. So, this explains why no change in the pedestal stability is observed.

Nonetheless, the pedestal pressure predicted by EPED1 has a clear increase with decreasing collisionality (figure 8(a)). This is because α_{max} is proportional to the pressure gradient and inversely proportional to ψ square via the volume derivative and pressure derivative (so inversely proportional to I_p square): $\alpha_{max} \propto p'/I_p^2$. Basically, with the same pedestal stability, higher plasma current can sustain a higher pedestal pressure. In the present dataset, the plasma current is increased at low collisionality in order to maintain ρ^* constant, The

current for the three plasmas of figure 8(*a*) is $I_p \approx 1.4$ MA, $I_p \approx 1.8$ MA and $I_p \approx 2.5$ MA for high, medium and low ν^*, respectively.

Experimentally, a change in the pedestal stability is observed instead. This is discussed in figure 8(*b*), where the experimental pressure gradient normalized to I_p^2 is shown. The normalized pressure gradient increases from ≈15 (kPa/psi/MA^2) at high ν^* to ≈30 (kPa/psi/MA^2) at low ν^*, showing an improvement in pedestal stability with decreasing collisionality. Note that the increase of the normalized pressure gradient with decreasing ν^* shown in figure 8(*b*) is due to the reduction of the pedestal width, figure 7(*b*). In fact, the dataset is selected to have constant β_p^{ped}, which implies constant p_e^{ped}/I_p^2. The EPED1-predicted pressure gradient normalized to I_p^2 instead shows no trend with collisionality.

In conclusion, while the experimental data show an improvement of the pedestal stability at low ν^*, the EPED1 predicts no difference in the pedestal stability with collisionality. The reason for the improvement of the pedestal stability is discussed in the next session.

6. Stability analysis

The pedestal stability of the experimental plasmas has been studied using ELITE to obtain the $j-\alpha$ stability diagram and the self-consistent path in the $j-\alpha$ space. Here, j is the current density and α is the normalized pedestal pressure gradient, as defined earlier. The equilibrium has been calculated using the HELENA code [79]. It uses as input the fit to the experimental T_e and n_e profiles selected in the pre-ELM phase. As described in section 2.3, the profiles are shifted in order to have $T_e^{sep} \approx 100$ eV. The edge bootstrap currents are calculated using the Koh model [77], which at high collisionality gives a more reliable result (i.e. closer to the results obtained with the drift kinetic code NEO [80, 81]) than with the more common approach described in [82]. Despite more accurate models of the bootstrap currents being recently developed (see for example [83]), the present results should still give a reasonable qualitative description of the pedestal stability.

To determine the stability boundary, two approaches have been used. (i) The normalized pressure gradient and the current density have been perturbed from the experimental values in order to obtain the $j-\alpha$ diagram with the stability boundary. This approach is useful to investigate the location of the operational point (i.e. the experimental j and α) in relation to the boundary. (ii) The height of the pedestal temperature is varied and the current profile is calculated self-consistently to find the marginally stable pedestal temperature height. This approach allows estimation of the self-consistent path in the $j-\alpha$ diagram starting from the operational point until the stability limit is reached and allows quantification of the α_{max} expected from the point of view of the peeling-ballooning stability model. In the stability calculation, modes from $n = 5$ up to $n = 70$ have been considered.

The results for a low and high collisionality case with same pedestal beta ($\beta_p^{ped} \approx 0.21$) are shown in figure 9. Note that

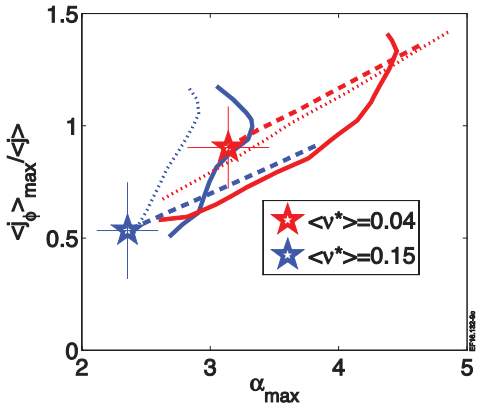

Figure 9. $j-\alpha$ stability diagram for low (red) and high (blue) collisionality plasmas with $\beta_p^{ped} \approx 0.21$. The stars show the operational point. The continuous lines show the stability boundary calculated with n up to 70. The thin dashed lines show the $n = \infty$ boundary. The thick dashed lines show the self-consistent path in the stability diagram.

the low ν^* plasma has a ballooning boundary with a shape that is reminiscent of a high triangularity plasma. However, this is not related to the fact that the low ν^* case has triangularity higher than the high ν^* case. The plasma shape is basically the same and the triangularity (averaged between upper and lower) is in the range $\delta \approx 0.24$–0.27 in both cases. The shape of the boundary for the low ν^* case shown in figure 9 is actually not uncommon in JET-ILW [18].

The stability analysis in figure 9 shows that the operational points are far from the $n = 70$ boundary (thick continuous line). This disagreement in not understood yet. It cannot be ascribed to the stability criterion used ($\gamma > 0.03\omega_A$ in the present work) as discussed in [18]. The disagreement is, however, consistent with the earlier stability analysis in JET-ILW [4, 18, 58]. In particular, the results described in [18] in low-δ JET-ILW plasmas at $I_p = 1.4$ MA $B_T = 1.7$ T and $\nu_{ped}^* \approx 0.3$–3 show that the operational point is near the $n = 70$ boundary at low D_2 gas injection ($\Gamma_{D2} \approx 0.3 \cdot 10^{22}$ e/s) while it is in the stable region at higher gas ($\Gamma_{D2} > 0.8 \cdot 10^{22}$ e/s). The present plasmas have $\Gamma_{D2} > 10^{22}$ (e/s), a value comparable to the high gas plasma in [18].

A source of discrepancy between the operational point and the stability boundary might be that the present modelling does not consider kinetic effects such as those related to the ion diamagnetic drift. These kinetic effects might affect the stability of an ideal ballooning mode [84] and further influence the stability boundary [85].

A further point to discuss is the uncertainty related to the experimental profile position. As described earlier, the profiles are shifted accordingly to a two-point model in order to have $T_e^{sep} \approx 100$ eV. In principle, small variations in T_e^{sep} might produce relevant changes in the stability boundary. To test the sensitivity of the stability boundary on T_e^{sep}, the stability analysis has been repeated by shifting the profiles in order to vary T_e^{sep} in the range 100–190 eV while keeping the other parameters (including the equilibrium) unchanged. The results are

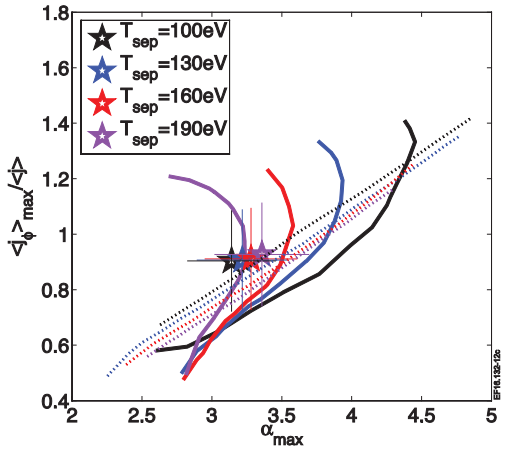

Figure 10. $j-\alpha$ stability diagram for a low-collisionality plasma ($\nu^*_{ped} \approx 0.01$) with $\beta_p^{ped} \approx 0.21$ shifting the experimental profiles in order to obtain a different separatrix temperature. The stars show the operational point. The continuous lines show the stability boundary calculated with up to $n = 70$. The thin dashed lines show the $n = \infty$ boundary.

summarized in figure 10 for the low ν^* case. The operational point is on the $n = 70$ stability boundary at $T_e^{sep} \approx 160\,eV$. This value seems too unrealistically high to conclude that the uncertainty in the experimental profile position might explain why the operational point is far from the boundary.

It is necessary to highlight that, for an accurate estimation of the boundary position, it might not be sufficient to consider only the modes up to $n = 70$. So, in figure 9 the $n = \infty$ boundary is shown with the thin dashed lines. In this case, the operational point is located on the $n = \infty$ boundary.

In conclusion, the stability analysis shows a good agreement with the experimental results when considering the $n = \infty$ boundary. When considering the $n = 70$ boundary, no quantitative agreement is observed; however, a reasonable qualitative agreement is present. In fact, the $n = 70$ boundary reaches higher normalized pressure at low ν^* than at high ν^*. Basically, the stability analysis suggests an improvement of the pedestal stability both considering the $n = \infty$ boundary and the $n = 70$ boundary.

This can be quantified for the $n = 70$ boundary by calculating the self-consistent path of the operational points. The thick dashed lines in figure 9 show the self-consistent path from the operational points to the corresponding $n = 70$ boundary. The intersection of the self-consistent path with the $n = 70$ boundary is used to determine the normalized pressure gradient expected by the stability analysis, α_{max}. The corresponding α_{max} versus collisionality are shown in figure 11(a) (pink asterisks). A clear reduction of α_{max} with increasing ν^* is present. For comparison, figure 11(a) also shows the normalized pressure gradient corresponding to the operational points of the experimental dataset (full symbols). A reduction of α with increasing collisionality is observed as well. Basically, both the experimental data and the stability analysis show that the pedestal stability improves with decreasing collisionality.

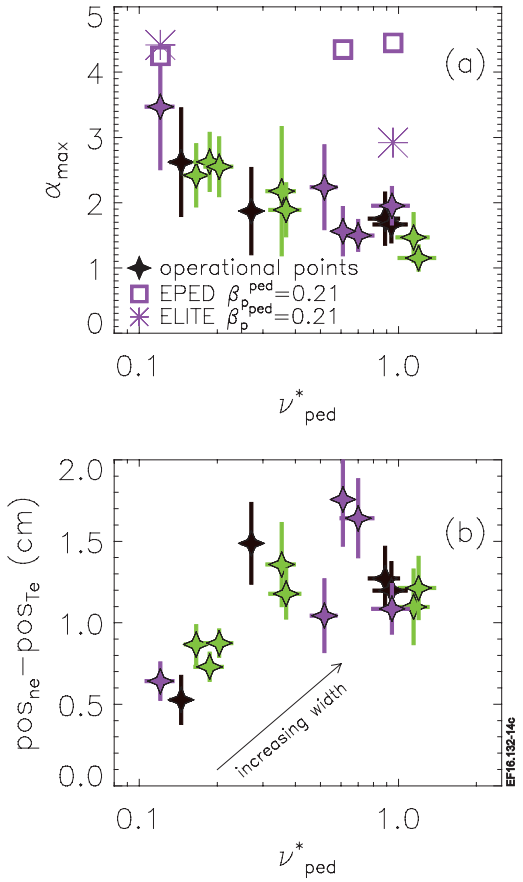

Figure 11. (a) α_{max} versus collisionality. Asterisks show the results of the *P-B* stability analysis, squares show the EPED1 value and the full symbols show the operational points for the experimental dataset. (b) Difference between T_e and n_e pedestal position versus collisionality calculated in real space (along the HRTS line of sight). In normalized ψ_{pol}, the variation of the relative shift is from 1% at low ν^* to 4% at high ν^*.

The increase of α_{max} at low collisionality (i.e. the pedestal stability improvement) is due to at least three factors.

(1) The pedestal is narrower at low collisionality than at high collisionality. The reduction of the pedestal width has a stabilizing effect on the pedestal [86].
(2) The difference in the position of the pedestal density and temperature is reduced with decreasing collisionality. This is shown in figure 11(b), where the difference in the positions versus collisionality is shown. The reduction of the relative shift between the n_e and T_e pedestal position with decreasing ν^* has a stabilizing effect on the pedestal [59].
(3) The reduction of collisionality leads to higher bootstrap current and hence moves the operational point upwards. The first two effects improve the stability at low collisionality and move the boundary to higher α_{max}. Then, the third effect tends to move the intersection of the boundary with the self-consistent path to further higher α_{max}.

Note that α_{max} estimated using the EPED1 model does not show any variation with collisionality, figure 11(a). This is because EPED1 does not use the experimental pressure profiles. In particular, in EPED1 (i) the width is estimated from

the KBM constraint and (ii) it is assumed there is no relative shift between the density and temperature. In fact, at low collisionality, where the pedestal width is consistent with the KBM constraint and the relative shift is small, the PB stability and the EPED1 model obtain a similar α_{max}.

7. Electron density in the scrape-off layer

The collisionality scan affects not only the pedestal density height and width, but also the SOL density. Figure 12(*a*) shows the density profile for the high collisionality shot of the present dataset that shows the highest SOL density. In this case, the assumption $n_e^{SOL} = 0$ used in equation (8) to fit the experimental data is not optimal. No significant difference is observed in the SOL temperature within the experimental HRTS uncertainty (no better diagnostic is available for the measurement of the SOL temperature). The SOL temperature is not further discussed.

The *mtanh* function discussed in equation (8) cannot properly describe the density shape outside the separatrix for the highest collisionality shots. The standard *mtanh* function can be adapted in several ways to better fit the SOL density. The HRTS diagnostic shows a decrease of the SOL density moving outwards from the separatrix. This observation has been confirmed with the reflectometer and the Li-beam. So, a valid alternative for the density fits is to add an SOL slope to equation (8):

$$mtanh^{SOL}(r) = \frac{h}{2}\left(\frac{(1+s^{core}x)e^{x} - (1+s^{SOL})e^{-x}}{e^{x}+e^{-x}} + 1\right) \quad (11)$$

The comparison of the fits using equations (8) and (11) is shown in figure 12(*a*). The fit using equation (11) better reproduces the SOL density profile.

However, the SOL density has no direct impact on the result related to the stability analysis and to the pedestal width. Figure 12(*b*) shows the pressure gradient calculated using the two fitting functions, and no difference is observed. This is because the temperature is close to zero in the SOL, so the pressure is not significantly affected by a non-zero SOL density. Since no measurable difference is observed in the pressure gradient, no difference is expected in the stability analysis using the $mtanh^{SOL}$ function. However, we must highlight that this conclusion applies to the present plasmas, while in other machines or in other experimental scenarios, where the density pedestal might be more inward [87], a direct effect of the SOL density on the pressure gradient is possible.

The use of equation (11) can also affect the density width estimation. In fact, the bottom of the pedestal is slightly more inward with $mtanh^{SOL}$ than with the standard *mtanh* (see the vertical dashed lines in figure 12(*a*)). The correlation of the density width with the pedestal collisionality is shown in figure 12(*c*) using the standard *mtanh* (full symbols) and $mtanh^{SOL}$ (empty symbols). In general, the width estimated with $mtanh^{SOL}$ tends to be slightly narrower than the estimation with the standard *mtanh*. However, the positive trend

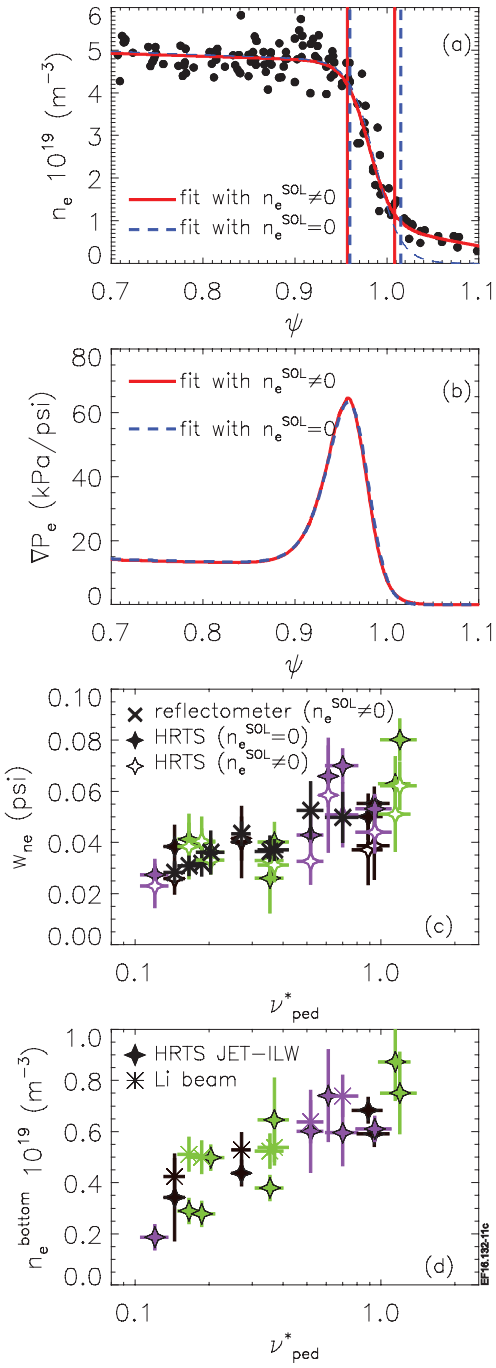

Figure 12. (*a*) electron density profile for a high ν^* shot (87 265) with the fit using *mtanh* and $mtanh^{SOL}$. The vertical lines highlight the pedestal width. (*b*) Corresponding pressure gradient. Density width estimated with standard *mtanh* and $mtanh^{SOL}$ (*c*) density at the bottom of the pedestal (*d*) versus collisionality.

with collisionality is still present and, within the experimental uncertainty, no major difference is observed.

The density width determined with the HRTS has been compared with that determined from the reflectometer. The reflectometer data have been fitted using the $mtanh^{SOL}$ function. When the reflectometer data were available, a reasonable agreement with the HRTS was observed (see the crosses in figure 12(*c*)).

The correlation between the density estimated at the pedestal bottom (n_e^{bottom}) versus the pedestal collisionality is shown in figure 12(*d*). n_e^{bottom} is calculated from the experimental data located in the region determined by the pedestal position plus half width (which roughly corresponds to the region of maximum curvature, see figure 12(*a*)). However, since the HRTS does not have an optimal spatial resolution in the SOL region, the estimation of n_e^{bottom} from the HRTS has been compared with the Li-beam, when available. In this dataset, the Li-beam can cover only the SOL and part of the pedestal region, so it cannot be used to estimate the pedestal width. For the Li-beam, n_e^{bottom} is calculated from the experimental data located around the region of maximum curvature at the pedestal bottom. Figure 12(*d*) shows a clear increase in n_e^{bottom} with collisionality. As discussed in figure 12(*b*), this behaviour does not have a direct measureable impact on the pressure gradient. However, we can speculate that the high n_e^{bottom} at high collisionality might cool down the SOL, reducing the SOL temperature. These combined effects might increase the SOL collisionality and consequently affect the bootstrap current at the separatrix which, in turn, might affect the pedestal stability. So, we cannot exclude the possibility that the reduction of the pedestal stability with increasing collisionality is also related to the increase in SOL density. Due to the lack of good experimental temperature measurements in the SOL, however, further claims are not possible. Further investigations might rely on a detailed modelling work, for example as recently done for the N_2 seeding plasma [49] using the EDGE2D-EIRENE code [88, 89].

8. Discussion and conclusions

This work shows that in JET-ILW a strong correlation between the confinement and the collisionality is present. While at high collisionality the confinement is low, with $H_{98} \approx 0.8$, at low collisionality JET-ILW can reach high confinement, with $H_{98} \approx 1.0$, comparable to JET-C.

Note that the increase of the confinement cannot be ascribed to an impurity effect. In particular, the divertor configuration used in this work has the outer strike point near the pump duct, on tile 6. Tile 6 is tungsten-coated and, in case of damage to the coating, there might be concern that the increase in the confinement could be somehow related to the increase in the carbon content in the plasma. For example, recent results on AUG have shown that carbon seeding can increase the confinement in a metal wall machine [90]. However, the carbon content is very low in JET-ILW, with a carbon concentration in the core of approximately 0.1% [91, 92], one order of magnitude lower than in JET-C [93]. In particular, the shots of this work with the best confinement have a carbon concentration in the core of approximately 0.15%, which is consistent with the estimation in [91] and still significantly lower than in JET-C. In the pedestal it is slightly higher, approximately 0.25%, but still significantly lower than in JET-C. Such levels of carbon concentration are characteristic of the JET-ILW plasmas in the very first ILW campaign and can be considered close the lowest carbon level feasible in JET-ILW.

The present JET-ILW results show a stronger scaling with collisionality (with a scaling exponent $\alpha_\nu \approx 0.6$) than the earlier JET-C results ($\alpha_\nu \approx 0.35$). If the difference is due to an effect related to the metal wall, this could provide important information for extrapolations to ITER. However, although the increase of the normalized energy confinement with decreasing ν^* has been observed in several devices, the quantitative trends have shown a relatively large variation. JET-C and JT60-U have shown a scaling of the normalized energy confinement $B\tau_E \propto \nu^{*-\alpha_\nu}$ with $\alpha_\nu \approx 0.35$ [25, 28]. DIII-D, at low collisionality, has shown a scaling comparable to JET-C, while a stronger scaling was observed at higher collisionality with $\alpha_\nu \approx 0.56$ [27]. The strongest scalings have been observed in Alcator C-Mod, with $\alpha_\nu \approx 0.75$ [24], in MAST, with $\alpha_\nu \approx 0.8$ [31] and in NSTX, with $\alpha_\nu \approx 0.8$–1.2 [33]. Most of these results have been summarized in [19] where it is empirically shown that the variation in the scaling exponent α_ν seems related to the collisionality itself, with stronger scalings observed at high collisionality. The present JET-ILW dataset, with core collisionality in the range ν^*(core) ≈ 0.04–0.2 and an exponent $\alpha_\nu \approx 0.6$, has a scaling comparable to the high-ν^* case in DIII-D and fits well within the empirical trend of α_ν versus ν^* discussed in [19]. So, the difference in the scaling exponent between the earlier JET-C results and the present JET-ILW results might be related to the fact that the JET-ILW scan has been performed in a collisionality range higher than the JET-C scan (which was in the range ν^*(core) ≈ 0.005–0.1). It is possible, then, that the stronger scaling of JET-ILW might have no major implications for ITER.

The JET-ILW collisionality scan shows that the increase of confinement at low collisionality is driven both by the increase in the core and in the pedestal pressure. At the pedestal, the reduction of the density is compensated by a stronger increase of the temperature, which leads to an increased pressure. In the core, the increased pressure is due to two factors: (i) the increase of T_e^{ped} leads to the increase of T_e^{core} via the T_e profile stiffness, and (ii) the reduced collisionality leads to higher density peaking and higher pressure peaking, further increasing the role of the core with respect to the pedestal.

In the pedestal region, a clear increase of the stability with decreasing ν^* is observed. The peeling-ballooning stability analysis shows that the improvement is due to at least three factors: (i) the reduction of the pedestal width at low ν^* (ii) the lower relative shift between density and temperature pedestal position and (iii) the increase in the bootstrap current at low ν^*. The trend of the pedestal stability with collisionality is, in principle, favourable for ITER, which is supposed to operate at low ν^*. However, the experimental results show that the relative shift has an impact on the stability while, at present, models that describes the relative shift have not yet been developed. It is necessary to understand how to model the relative shift before a quantitative extrapolation to ITER.

A significant change in the pedestal structure has been observed. In particular, the pedestal width narrows with decreasing collisionality. The reason for the pedestal width

scaling with collisionality is still unclear and this behaviour is not well reproduced by the scaling implemented in the EPED1 model. This suggests that the present models for the pedestal width estimation might not be sufficient to describe the pedestal behaviour in detail. Nonetheless, at low collisionality a good agreement with the experimental data is observed within 10–15%. An extrapolation to ITER collisionalities suggests that the trend of the pedestal width versus ν^* is likely not to have a major effect on the present ITER width estimations.

From the point of view of the pedestal height, the EPED1 model shows a trend with collisionality that is qualitatively similar to the experimental data. However, the EPED1 trend is due only to the higher plasma current used in the low ν^* plasmas and no significant changes in the EPED1 pedestal stability are observed. At low collisionality, where the EPED1 pedestal width is consistent with the experimental results, the EPED1-predicted pedestal stability is in agreement with the α_{max} determined with the P-B stability analysis. At high collisionality, the EPED1-predicted α_{max} is significantly higher than the α_{max} determined from the P-B stability. At high collisionality, EPED1 can still predict the pedestal pressure height reasonably well because its overestimated α_{max} is compensated by the underestimated pedestal pressure width.

The experimental results suggest that the SOL might play a role in the pedestal stability. Including the effects in the SOL might be necessary to reach a more reliable description of the pedestal physics. The role of the neutrals might also be important as they might affect the density pedestal position and hence the pedestal stability. Further investigations on this point are necessary.

Acknowledgement

This work has been carried out within the framework of the EUROfusion Consortium and has received funding from the Euratom research and training programme 2014–2018 under grant agreement No 633053. The views and opinions expressed herein do not necessarily reflect those of the European Commission.

References

[1] Brezinszek S. *et al* 2012 *Proc. 24th Int. Conf. on Fusion Energy (San Diego, 2012)* p EX/4-1 (www-naweb.iaea.org/napc/physics/FEC/FEC2012/index.htm)
[2] Matthews G. *et al* 2013 *J. Nucl. Mater.* **438** S2
[3] Giroud C. *et al* 2013 *Nucl. Fusion* **53** 113025
[4] Beurskens M. *et al* 2014 *Nucl. Fusion* **54** 043001
[5] ITER Physics Basis 1999 *Nucl. Fusion* **39** 2175
[6] Nunes I. *et al* 2014 *25th IAEA Fusion Energy Conf. (St. Petersburg, 2014)* p EX/9-2 (http://www-naweb.iaea.org/napc/physics/FEC/FEC2012/html/fec12.htm)
[7] Nunes I. *et al* 2015 *42th EPS Conf. on Plasma Physics (Lisbon, Portugal, 2015)* p O1.001 (http://ocs.ciemat.es/EPS2015PAP/html/)
[8] Nunes I. 2016 *Plasma Phys. Control. Fusion* **58** 014034
[9] Saibene G. *et al* 2002 *Plasma Phys. Control. Fusion* **44** 1769
[10] Nunes I. *et al* 2013 *Plasma Phys. Control. Fusion* **53** 073020
[11] Beurskens M. *et al* 2003 *Nucl. Fusion* **53** 013001
[12] de la Luna E. *et al* 2014 Comparative study of high triangularity H-mode plasma performance in JET with Be/W wall and CFC wall EX/P5-195 *Paper Presented at 25th IAEA Int. Conf. on Fusion Energy (St. Petersburg, 2014)* (www-pub.iaea.org/iaeameetings/46091/25th-Fusion-Energy-Conference-FEC-2014)
[13] Giroud C. *et al* 2015 *Plasma Phys. Control. Fusion* **57** 035004
[14] Frassinetti L. *et al* 2015 *Nucl. Fusion* **55** 023007
[15] Schweinzer J. *et al* 2011 *Nucl. Fusion* **51** 113003
[16] Schneider P.A. *et al* 2015 *Plasma Phys. Control. Fusion* **57** 014029
[17] Joffrin E. *et al* 2014 *Proc. 25th Int. Conf. on Fusion Energy (St. Petersburg, 2014)* p EX/P5-40 (www-pub.iaea.org/iaeameetings/46091/25th-Fusion-Energy-Conference-FEC-2014)
[18] Maggi C. *et al* 2015 *Nucl. Fusion* **55** 113031
[19] Luce T.C. Petty C.C. and Cordey J.C. 2008 *Plasma Phys. Control. Fusion* **50** 043001
[20] Kadomstev B.B. 1975 *Sov. J. Plasma Phys.* **1** 295
[21] Bourdelle C. 2011 *Nucl. Fusion* **51** 063037
[22] Petty C.C. *et al* 1995 *Phys. Plasmas* **2** 2342
[23] Ryter F. *et al* 1997 *Fusion Energy Conf. (Montreal, 1996)* vol 1 p 625
[24] Greenwald M. *et al* 1998 *Plasma Phys. Control. Fusion* **40** 789
[25] Shirai H. *et al* 2000 *Plasma Phys. Control. Fusion* **42** 1193
[26] Cordey J.G. *et al* 2005 *Nucl. Fusion* **45** 1078
[27] Petty C.C. and Luce T.C. 1999 *Phys. Plasmas* **6** 909
[28] McDonald D.C. *et al* 2004 Fusion Energy *Proc. 20th Int. Conf. (Vilamoura, 2004)* (Vienna: IAEA) CD-ROM file EX6-6 and (www-naweb.iaea.org/napc/physics/fec/fec2004/datasets/index.html)
[29] McDonald D. *et al* 2004 *Plasma Phys. Control. Fusion* **46** A215
[30] Petty C.C. 2004 *et al Phys. Plasmas* **11** 2514
[31] Valovic M. 2011 *et al Nucl. Fusion* **51** 073045
[32] Petty C.C. *et al* 2012 *Proc. 24th Int. Conf. on Fusion Energy (San Diego, 2012)* p ITR/P1-30 (http://www-naweb.iaea.org/napc/physics/FEC/FEC2012/html/fec12.htm)
[33] Kaye S.M. *et al* 2013 *Nucl. Fusion* **53** 063005
[34] Angioni C. *et al* 2009 *Phys. Plasmas* **16** 060702
[35] Angioni C. *et al* 2003 *Phys. Rev. Lett.* **90** 205003
[36] Valovic M. *et al* 2004 *Plasma Phys. Control. Fusion* **46**
[37] Weisen H. *et al* 2006 *Plasma Phys. Control. Fusion* **48** A457
[38] Greenwald M. *et al* 2007 *Nucl. Fusion* **47** L26
[39] Takenaga H. *et al* 2008 *Nucl. Fusion* **48** 075004
[40] Shimada M. *et al* 2007 *Nucl. Fusion* **47** S1
[41] Kinsey J.E. *et al* 2011 *Nucl. Fusion* **51** 083001
[42] Wilson H.R. *et al* 2002 *Phys. Plasmas* **9** 1277
[43] Snyder P.B. *et al* 2002 *Phys. Plasmas* **9** 2037
[44] Huysmans G.T.A. *et al* 2005 *Plasma Phys. Control. Fusion* **47** B165
[45] Saarelma S. *et al* 2009 *Plasma Phys. Control. Fusion* **51** 035001
[46] Groebner R.J. *et al* 2013 *Nucl. Fusion* **53** 093024
[47] Konz C. *et al* 2011 *EPS Conf. on Plasma Physics (Strasbourg, France, 2011)* p O2.10 (http://ocs.ciemat.es/EPS2011PAP/pdf/O2.103.pdf)
[48] Urano H. *et al* 2014 *Nucl. Fusion* **54** 116001
[49] Saarelma S. *et al* 2015 *Phys. Plasmas* **22** 056115
[50] Wolfrum E. *et al* 2014 *Nucl. Fusion* **55** 053017
[51] Snyder P.B. *et al* 2009 *Phys. Plasmas* **16** 056118
[52] Kirk A. *et al* 2004 *Plasma Phys. Control. Fusion* **46** A187
[53] Urano H. *et al* 2008 *Nucl. Fusion* **48** 103016
[54] Maggi C. *et al* 2010 *Nucl. Fusion* **50** 025023
[55] Beursknes M.N.A. *et al* 2011 *Phys. Plasmas* **18** 056120
[56] Walk J.R. *et al* 2012 *Nucl. Fusion* **52** 063011
[57] Diallo A. *et al* 2011 *Nucl. Fusion* **51** 103031
[58] Leyland M. *et al* 2015 *Nucl. Fusion* **55** 013019

[59] Beursknes M.N.A. *et al* 2009 *Plasma Phys. Control. Fusion* **51** 124051
[60] Groebner R.J. *et al Nucl. Fusion* **44** 204
[61] Onjun T. *et al* 2002 *Phys. Plasmas* **9** 5018
[62] Leyland M. *et al* 2013 *Nucl. Fusion* **53** 083028
[63] Urano H. *et al* 2015 *42th EPS Conf. on Plasma Physics (Lisbon, Portugal, 2015)* p P5.146 (http://ocs.ciemat.es/EPS2015PAP/pdf/P5.146.pdf)
[64] Urano H. *et al* 2016 *Nucl. Fusion* **56** 016005
[65] Loarte A. *et al* 2003 *Plasma Phys. Control. Fusion* **45** 1549
[66] de Vries P.C. *et al* 2008 *Nucl. Fusion* **48** 065006
[67] Petty C.C. *et al* 1997 *Nucl. Fusion* **37** 1
[68] Pasqualotto R. *et al* 2004 *Rev. Sci. Instrum.* **75** 3891
[69] Groebner R.J. *et al* 2001 *Nucl. Fusion* **41** 1789
[70] Kallenbach A. *et al* 2005 *J. Nucl. Mater.* **337–9** 381
[71] Frassinetti L. *et al* 2012 *Rev. Sci. Instrum.* **83** 013506
[72] Sirinelli A. *et al* 2010 *Rev. Sci. Instrum.* **81** 10D939
[73] Cordey J.G. *et al* 2004 *Proc. 31st EPS Conf. on Plasma Physics (London, 2004)* vol 28G (ECA) p O1.05
[74] Maslov M. *et al* 2009 *Nucl. Fusion* **49** 075037
[75] Scannell R. *et al* 2011 *Rev. Sci. Instrum.* **82** 053501
[76] Verdoolaege G. 2015 *Entropy* **17** 4602
[77] Koh S. *et al* 2012 *Phys. Plasmas* **19** 072505
[78] Miller R.L. 1998 *Phys. Plasmas* **5** 973
[79] Huysmans G.T.A. *et al* 1991 *Computational Physics: Proc. Int. Conf. (Amsterdam, The Netherlands, 1991)* (Singapore: World Scientific)
[80] Belli E. *et al* 2012 *Plasma Phys. Control. Fusion* **54** 015015
[81] Belli E. *et al* 2014 *Plasma Phys. Control. Fusion* **56** 045006
[82] Sauter O. and Angioni C. 1999 *Phys. Plasmas* **6** 2834
[83] Hager R. 2016 *Phys. Plasmas* **23** 042503
[84] Hastie R.J. Ramos J.J. and Porcelli F. 2003 *Phys. Plasmas* **10** 4405
[85] Aiba N. and Oyama N. 2012 *Nucl. Fusion* **52** 114002
[86] Snyder P.B. *et al* 2011 *Nucl. Fusion* **51** 103016
[87] Wolfrum E. *et al* 2015 *42th EPS Conf. on Plasma Physics (Lisbon, Portugal, 2015)* p P1.115 (http://ocs.ciemat.es/EPS2015PAP/pdf/P1.115.pdf)
[88] Reiter D. 1992 *J. Nucl. Mater.* **88** 196
[89] Simonini R. *et al* 1994 *Contrib. Plasma Phys.* **34** 368
[90] Beurskens M. *et al* 2016 *Nucl. Fusion* **56** 056014
[91] Brezinsek S. *et al* 2015 *J. Nucl. Mater.* **463** 11
[92] Brezinsek S. *et al* 2013 *J. Nucl. Mater.* **438** S303
[93] Brezinsek S. *et al* 2015 *Nucl. Fusion* **55** 063021
[94] Romanelli F. *et al* 2015 *Nucl. Fusion* **55** 104001